

See discussions, stats, and author profiles for this publication at: <https://www.researchgate.net/publication/7029934>

# EPR Spectroscopic and Computational Characterization of the Hydroxyethylidene-Thiamine Pyrophosphate Radical Intermediate of Pyruvate:Ferredoxin Oxidoreductase †

ARTICLE in BIOCHEMISTRY · JULY 2006

Impact Factor: 3.02 · DOI: 10.1021/bi0602516 · Source: PubMed

CITATIONS

33

READS

34

9 AUTHORS, INCLUDING:



[Steven Mansoorabadi](#)

Auburn University

25 PUBLICATIONS 421 CITATIONS

[SEE PROFILE](#)



[Javier Seravalli](#)

University of Nebraska at Lincoln

51 PUBLICATIONS 1,423 CITATIONS

[SEE PROFILE](#)



[Cristina M Furdul](#)

Wake Forest School of Medicine

58 PUBLICATIONS 866 CITATIONS

[SEE PROFILE](#)



[Stephen W Ragsdale](#)

University of Michigan

201 PUBLICATIONS 7,460 CITATIONS

[SEE PROFILE](#)

Published in final edited form as:

Biochemistry. 2006 June 13; 45(23): 7122–7131.

# EPR Spectroscopic and Computational Characterization of the Hydroxyethylidene-Thiamine Pyrophosphate Radical Intermediate of Pyruvate:Ferredoxin Oxidoreductase †

Steven O. Mansoorabadi<sup>†</sup>, Javier Seravalli<sup>§</sup>, Cristina Furdui<sup>§,||</sup>, Vladimir Krymov<sup>⊥</sup>, Gary J. Gerfen<sup>⊥</sup>, Tadhg P. Begley<sup>#</sup>, Jonathan Melnick<sup>#</sup>, Stephen W. Ragsdale<sup>§</sup>, and George H. Reed<sup>\*,‡</sup>

<sup>‡</sup>Department of Biochemistry, University of Wisconsin-Madison, Madison, WI 53726-4087

<sup>§</sup>Department of Biochemistry, University of Nebraska, Lincoln, NE 68588-0664

<sup>⊥</sup>Department of Physiology & Biophysics, Albert Einstein College of Medicine, Bronx, NY 10461-1602

<sup>#</sup>Department of Chemistry and Chemical Biology, Baker Laboratory, Cornell University, Ithaca, NY 14853

## Abstract

The radical intermediate of pyruvate:ferredoxin oxidoreductase (PFOR) from *Moorella thermoacetica* was characterized using electron paramagnetic resonance (EPR) spectroscopy at X-band and D-band microwave frequencies. EPR spectra obtained with various combinations of isotopically labeled substrate (pyruvate) and coenzyme (thiamine pyrophosphate (TPP)), were analyzed by spectral simulations. Parameters obtained from the simulations were compared with those predicted from electronic structure calculations on various radical structures. The *g*-values and <sup>14</sup>N/<sup>15</sup>N-hyperfine splittings obtained from the spectra are consistent with a planar, hydroxyethylidene-thiamine pyrophosphate (HE-TPP)  $\pi$ -radical, in which spin is delocalized onto the thiazolium sulfur and nitrogen atoms. The <sup>1</sup>H-hyperfine splittings from the methyl group of pyruvate and the <sup>13</sup>C-hyperfine splittings from C2 of both pyruvate and TPP are consistent with a model in which the pyruvate-derived oxygen atom of the HE-TPP radical forms a hydrogen bond. The hyperfine splitting constants and *g*-values are not compatible with those predicted for a non-planar,  $\sigma$ /n-type cation radical.

Pyruvate:ferredoxin oxidoreductase (E.C.1.2.7.1) (PFOR<sup>1</sup>) is a member of the 2-keto acid oxidoreductase family. This enzyme plays a central role in anaerobic fermentative metabolism by catalyzing the reversible, CoA-dependent, oxidative decarboxylation of pyruvate to acetyl-CoA and CO<sub>2</sub> (3). The two electrons generated in the oxidative reaction are transferred through [4Fe-4S] clusters in PFOR to an oxidized ferredoxin (4). PFOR is found in microbes lacking mitochondria from all three kingdoms (5). PFOR enzymes from different species have been grouped into three types depending on subunit composition (6). The different types of PFOR enzymes have between one and three [4Fe-4S] clusters. The [4Fe-4S] clusters are electron transfer cofactors serving as way-stops for electrons exiting the active site in the forward

<sup>†</sup>This work was supported by grants from the National Institutes of Health: GM35752 G.H.R.; GM39451 S.W.R.; DK44083 T.P.B.; and Center Grant 1P20RR17675 to the University of Nebraska. S.O.M. was supported by an NIH Predoctoral Training Grant T32 GM 08293.

\*To whom correspondence should be addressed. Telephone: (608) 262-0509; Fax: (608) 265-2904; Email: reed@biochem.wisc.edu.

<sup>||</sup>Current address: Department of Pharmacology, Yale University School of Medicine, New Haven, CT 06520-8066

<sup>1</sup>Abbreviations: PFOR, pyruvate:ferredoxin oxidoreductase; CoA, coenzyme A; TPP, thiamine pyrophosphate; HE-TPP, hydroxyethylidene-thiamine pyrophosphate; EPR, electron paramagnetic resonance; ENDOR, electron nuclear double resonance; CW, continuous wave; DFT, density functional theory; S/N, signal-to-noise ratio; RMSD, root mean square deviation; POX, pyruvate oxidase.

reaction (7). PFOR from *Moorella thermoacetica* is homodimeric and contains one molecule of TPP and three [4Fe-4S] clusters per subunit. Structures for a similar PFOR from *Desulfovibrio africanus* have revealed the location of the active site and the positions of the three [4Fe-4S] clusters (4,7).

Whenever PFOR from *Halobacterium halobium* was incubated with pyruvate in the absence of CoA, a persistent radical intermediate was detected by EPR spectroscopy (8). This radical was attributed to a one-electron oxidized, radical form of HE-TPP (8,9). The kinetic competence of the analogous HE-TPP radical in the reaction of *M. thermoacetica* PFOR was subsequently demonstrated (10). Thus, in the absence of CoA, the radical appears at a rate  $\sim 3$  fold greater than  $k_{\text{cat}}$ , and upon addition of CoA, the radical decays at a rate  $\gg k_{\text{cat}}$  giving rise to the normal products of the reaction (10). Despite differences in subunit composition and in the number of [4Fe-4S] clusters among PFOR's from different organisms, it is likely that oxidation of the HE-TPP intermediate occurs in two single-electron steps in most, if not all PFOR's (10). This view is supported by careful inspection of EPR spectra published for the HE-TPP radical intermediate of PFOR's from *M. thermoacetica* (10), *D. africanus* (11), *H. halobium* (12), and *Methanosarcina barkeri* (13). The EPR spectra recorded for the HE-TPP radical intermediate of these four different PFOR's exhibit identical hyperfine splitting patterns. The EPR results show that the radicals from the different enzymes have the same distribution of unpaired spin and therefore the same electronic structure.

Experiments with  $[3\text{-}^2\text{H}_3]\text{pyruvate}$  yielded an EPR spectrum with modestly narrowed line width, which indicated that the methyl protons of the substrate contribute hyperfine splitting to the radical EPR signal (10). A modest influence of  $[2\text{-}^{13}\text{C}]\text{pyruvate}$  on EPR spectra of the intermediate in PFOR from *M. barkeri* was reported, but the  $^{13}\text{C}$  effects were not evaluated quantitatively (13). ENDOR spectroscopy was also used to study the pyruvate-derived radical in the *M. thermoacetica* enzyme (2). These experiments detected  $^1\text{H}$ - and  $^2\text{H}$ -hyperfine coupling from samples of PFOR prepared with pyruvate and with  $[3\text{-}^2\text{H}_3]\text{pyruvate}$ , respectively. In addition, CW ENDOR revealed a weak, isotropic  $^{31}\text{P}$ -hyperfine coupling from the pyrophosphate moiety of the TPP cofactor. The ENDOR data were interpreted in terms of two possible models for the radical intermediate—an acetyl  $\sigma$ -type radical intimately associated with TPP or a  $\pi$ -type radical wherein the unpaired spin was delocalized over the thiazolium ring (2). The delocalized  $\pi$ -type radical structure for this intermediate had been suggested earlier (14).

Questions regarding the electronic structure of the radical have arisen from a recent X-ray crystallographic investigations of PFOR from *D. africanus* (11,15). Crystals lacking CoA were soaked with pyruvate prior to freezing and data collection. EPR spectra of similarly treated crystals revealed that the radical intermediate state was achieved. Electron density in the active site suggested that the thiazolium ring of TPP was bent and that there was a long bond (1.95 Å and 1.75 Å for the two independent PFOR molecules in the asymmetric unit) between C2 of the thiazolium ring and C2 $\alpha$ , of the substrate-derived moiety. These structural features of the intermediate were interpreted in terms of an unusual  $\sigma/\pi$ -type cation radical (11,15).

Addition of CoA to solutions of the radical intermediate complex of PFOR dramatically accelerates the decay of the intermediate (10). Several mechanisms have been suggested for the subsequent steps leading to further oxidation of the HE-TPP radical, production of acetyl-CoA, and transfer of the second electron into the [4Fe-4S] electron transfer conduit (3,16). Among these proposals are: 1) oxidation of CoA to a thiyl radical and subsequent radical combination with the HE-TPP radical; 2) CoA-gated further oxidation of the HE-TPP radical to acetyl-TPP, followed by nucleophilic attack by the CoA thiolate; 3) nucleophilic addition of the CoA thiolate to the HE-TPP radical to form a radical anion that subsequently transfers an electron to the proximal [4Fe-4S] cluster (10); 4) fragmentation of the  $\sigma/\pi$ -type cation radical

to an acetyl radical followed by radical recombination with a CoA-thiyl radical (11). Elucidation of the structure of the HE-TPP radical intermediate is essential to an eventual understanding of the subsequent steps in the overall reaction of PFOR. A more detailed EPR investigation of the radical intermediate in PFOR was therefore initiated in order to gain a clearer understanding of the electronic structure of this species through EPR measurements of the distribution of unpaired spin. In addition, the electronic structure of the radical was explored with electronic structure calculations using *Gaussian 98* (17) and ORCA 2.4-41 (18).

## Materials and Methods

### Preparation of labeled TPP and pyruvate

4-methyl-5-( $\beta$ -hydroxyethyl)thiazole labeled with  $^{15}\text{N}$  at N3 ( $[3-^{15}\text{N}]\text{TPP}$ ) or  $^{13}\text{C}$  at C2 ( $[2-^{13}\text{C}]\text{TPP}$ ) of the thiazole ring was prepared by condensing 3-chloro-4-oxopentyl acetate with either  $^{15}\text{N}$ - or  $^{13}\text{C}$ -labeled thioformamide, followed by acidic hydrolysis(19,20). The isotopically labeled thiazole compound was then converted to TPP using the previously described enzymatic synthesis (21). The presence of the isotopic labels was confirmed by mass spectrometry ( $\text{MW} = 426 \text{ g mol}^{-1}$ ).

$[3-^2\text{H}_3]\text{Pyruvate}$  was prepared by overnight incubation of  $\sim 3 \text{ g}$  of unlabeled pyruvic acid in  $0.10 \text{ L}$  of  $^2\text{H}_2\text{O}$  from Isotec (Sigma-Aldrich, St. Louis, MO) at  $110^\circ\text{C}$  in a sealed, high-pressure bottle. The reaction mixture was concentrated by roto-evaporation under vacuum, followed by vacuum distillation of  $^2\text{H}_4$ -pyruvic acid. Sodium  $[3-^2\text{H}_3]\text{pyruvate}$  was prepared by recrystallization in a  $\text{NaOH}/\text{ethanol}$  mixture, followed by lyophilization.  $[2-^{13}\text{C}]\text{Pyruvate}$  and  $[3-^{13}\text{C}]\text{pyruvate}$  were purchased from Cambridge Isotopes (Andover, MA). All other chemicals were obtained from Sigma-Aldrich.

### Reconstitution of PFOR with labeled TPP

Purification of PFOR is routinely carried out in the presence of  $1 \text{ mM}$  TPP and  $2 \text{ mM}$   $\text{MgCl}_2$ . It was found that removal of these two compounds led to the loss of PFOR activity without loss of  $[4\text{Fe-4S}]$  clusters from the protein. Furthermore, addition of TPP and  $\text{MgCl}_2$  at  $\text{pH} < 8.0$  reconstituted the PFOR activity to  $> 90\%$ . A method could therefore be developed to remove the bound TPP from PFOR and reconstitute the enzyme with labeled TPP. To remove bound TPP from PFOR,  $2.4 \text{ mg/ml}$  PFOR in  $50 \text{ mM}$  Tris/HCl,  $\text{pH} = 8.6$ , was dialyzed for a total of  $4 \text{ h}$  against two changes of  $0.5 \text{ L}$  of the same buffer. Removal of TPP from PFOR was monitored using the standard assay buffer for PFOR activity but omitting TPP and  $\text{MgCl}_2$ . The assay contained  $50 \text{ mM}$  MOPS/NaOH,  $\text{pH} = 7.5$ ;  $2 \text{ mM}$  DTT;  $1 \text{ mM}$  CoA;  $10 \text{ mM}$  pyruvate; and  $8 \text{ mM}$  methyl viologen (MV) at  $55^\circ\text{C}$ . More than  $95\%$  of the dialyzed PFOR was considered to be TPP-free based on the specific activity as measured by the modified assay. After concentration of the enzyme to  $3.2 \text{ mg mL}^{-1}$ ,  $0.4 \text{ mL}$  of PFOR was dialyzed against  $50 \text{ mM}$  Tris/HCl,  $\text{pH} = 7.4$ . After dialysis, each sample of TPP-free PFOR was subjected to a TPP reconstitution step.  $2 \mu\text{L}$  aliquots of  $10 \text{ mM}$   $^{15}\text{N}$ - or  $^{13}\text{C}$ -labeled TPP and  $20 \text{ mM}$   $\text{MgCl}_2$  stock solutions (made in the same buffer as the enzyme to be reconstituted) were added to the PFOR solution. The solution was allowed to equilibrate for  $10 \text{ min}$ , and the specific activity was measured using the TPP-free reaction mixture described above. The addition of TPP was stopped when the specific activity became constant ( $0.5\text{-}1 \text{ mM}$  TPP).

### Preparation of samples for EPR measurements

PFOR ( $100 \mu\text{M}$ ) in  $50 \text{ mM}$  Tris/HCl  $\text{pH} 7.4$  containing  $2 \text{ mM}$  DTT,  $2 \text{ mM}$   $\text{MgCl}_2$ , and either  $1 \text{ mM}$  unlabeled TPP or between  $0.5\text{-}1 \text{ mM}$  labeled TPP was reacted with  $10 \text{ mM}$  labeled or unlabeled pyruvate. The reaction was stopped after  $1 \text{ min}$  by immersion of the tube in liquid nitrogen. X-band EPR spectra were collected immediately after the samples were frozen. The X-band spectra were recorded with a Bruker ESP300e/EMX spectrometer. Sample temperature

was maintained at  $80 \pm 3$  K with an Oxford Instruments continuous flow Helium cryostat model ESR 900. The double integrals of the EPR signals were compared to that of a 1.1 mM Cu (ClO<sub>4</sub>)<sub>2</sub> standard to determine the number of spins per monomer. Power saturation analysis was performed to ensure that the signals were not saturated under the experimental conditions. Spin concentrations between  $\sim 0.1$ -0.2 HE-TPP radical/monomer were obtained with all of the samples. Scan averaging was used to collect the spectra with high S/N. For X-band spectra, resolution of hyperfine splitting was enhanced by Fourier methods (22,23).

### High-field EPR spectroscopy

D-Band (130 GHz) EPR spectra were acquired on a spectrometer assembled at Albert Einstein College of Medicine. The magnetic field is generated by a specially designed, 7 Tesla superconducting magnet with a  $\pm 0.5$  Tesla superconducting sweep/active shielding coil. The quadrature detection microwave bridge, capable of generating 100 mW pulses at its output, was designed and built by HF EPR Instruments, Inc. (V. Krymov, New York). The probe uses cylindrical resonators operating in the TE<sub>011</sub> mode and slotted to allow penetration of RF fields used in ENDOR. Typical  $\pi/2$  pulse widths of 30-50 ns can be achieved with the available power. Samples were contained in quartz capillary tubes with outer and inner diameters of 0.6 mm and 0.5 mm, respectively, and an active volume of 0.2  $\mu$ L. Field-swept two-pulse echo-detected spectra were obtained because CW spectra suffered from saturation effects even at high temperatures and low microwave powers. To facilitate field calibration and maximize sensitivity, the echo detected spectra were acquired with 10 G, 300 Hz square-wave field modulation, yielding the derivative presentation directly from the spectrometer without further need for data manipulation. The magnetic field was calibrated to an accuracy of  $\sim 3$  G using a sample of Mn doped into MgO (24). The temperature of the sample was maintained to an accuracy of approximately  $\pm 0.3^\circ$  using an Oxford Spectrostat continuous-flow cryostat and ITC503 temperature controller. Specific experimental parameters are given in figure legends.

### Spectral Simulations

The EPR spectra were analyzed using the following spin Hamiltonian:

$$H = \beta B \cdot g \cdot S + \sum_i (I_i \cdot A_i \cdot S) \quad (1)$$

The first term in eq 1 represents the Zeeman interaction of the HE-TPP radical with the external magnetic field. The second term represents a sum of the relevant nuclear hyperfine interactions. The hyperfine interactions were treated to first-order which makes the energy matrix block diagonal in the nuclear spin quantum number,  $m_I$ . Strategies for the simulation of field-swept powder EPR spectra were described previously (25). The  $g$ -values and hyperfine splitting parameters were variables in the fitting procedure. Initially the EPR spectra obtained from samples prepared with [3-<sup>2</sup>H<sub>3</sub>]pyruvate and [3-<sup>15</sup>N]TPP (Figure 1A) and [3-<sup>2</sup>H<sub>3</sub>]pyruvate and unlabeled TPP (Figure 1B) were fitted simultaneously using <sup>14</sup>N/<sup>15</sup>N-hyperfine parameters scaled by their magnetogyric ratios. The  $g$ -values were determined by simulation of the corresponding high-field (D-band) EPR spectra (Figure 2) in which the three  $g$ -values are resolved. The  $g$ -values and hyperfine splitting parameters thus obtained were fixed and their influences incorporated into the simulations of the other spectra. The EPR spectrum obtained from samples prepared with unlabeled pyruvate and TPP (Figure 1C) were next analyzed and the <sup>1</sup>H-hyperfine splitting parameters obtained from the simulation were incorporated into the fixed parameter set. Finally, the EPR spectra acquired from samples prepared with <sup>13</sup>C-labeled pyruvate or TPP were simulated using the fixed parameter set and the <sup>13</sup>C-hyperfine parameters were obtained. The simulation parameters were refined by trial-and-error until reasonable fits and a self-consistent set of parameters were obtained. Because of the visual, trial-and-error nature of the fitting method, it is difficult to provide a rigorous estimate of the uncertainties in

the parameters. However, it is possible to determine peak positions to within  $\pm 1$  Gauss, and this is an “operational” error estimate for the hyperfine splitting parameters. Based on the precision of magnetic field measurement in the D-band spectra, the  $g$ -values have an error within  $\pm 0.0001$ .

## Electronic Structure Calculations

To aid in the interpretation of the parameters obtained from the EPR simulations, estimates for the  $g$ -values and hyperfine parameters of different truncated models of the HE-TPP radical were obtained from electronic structure calculations. These truncated models are shown in Scheme 1. Models 1 and 2 consist of the geometry-optimized structures of the protonated and unprotonated forms of the HE-TPP  $\pi$ -radical, respectively. Models 3 and 4 consist of the geometry-optimized structures of two different tautomers of the putative  $\sigma/n$ -type cation radical that were proposed to account for the electron density observed in the X-ray crystal structure of PFOR from *D. africanus* (11,15). Models 1'-4' consist of the same radical structures as the corresponding unprimed models, but with the positions of heavy atoms restricted to those reported in the crystal structure (PDB ID# 1KEK) (11).

Geometry optimizations and single-point hyperfine tensor calculations were performed on each model starting from the X-ray coordinates (PDB ID# 1KEK) of the HE-TPP radical using *Gaussian98* (17). Geometry optimizations were performed using Becke-style 3-Parameter Density Functional Theory (DFT) with the Lee-Yang-Parr correlation functional (B3LYP) and Pople's polarized double- $\zeta$  6-31G\* basis set. In the case of models 1'-4', the positions of heavy atoms assigned in the electron density maps from the crystal structure, were frozen during the geometry optimization and only the positions of the H-atoms were allowed to vary. RMSD's between the heavy atoms of the geometry-optimized structures (models 1 - 4) and the corresponding X-ray coordinates (models 1' - 4') were obtained by overlaying the structures and employing a simulated annealing algorithm (26) to minimize the differences in atomic coordinates.

Single-point calculations were then performed on the optimized structures using the B3LYP hybrid functional in combination with the DFT-optimized valence triple- $\zeta$  basis, TZVP, which has been shown to give accurate estimates for hyperfine parameters of nuclei from the first three rows of the periodic table (27,28). Estimates of the  $g$ -tensors of each model were obtained from single-point calculations with the ORCA 2.4-41 software package using the same B3LYP/TZVP scheme (18).

## Results and Discussion

### CW EPR Spectra of the HE-TPP Radical in PFOR

EPR spectra of samples of PFOR prepared with various combinations of isotopically labeled pyruvate and TPP are shown in Figure 1. Inspection of the spectra corresponding to samples made up with [2- $^{13}\text{C}$ ]pyruvate (Figure 1E) and with [2- $^{13}\text{C}$ ]TPP (Figure 1F) is immediately revealing.  $\sigma$ -Radicals typically exhibit  $^{13}\text{C}$ -hyperfine splittings of  $> 100$  G (29) whereas the substitution of  $^{13}\text{C}$  at each end of the C2-C2 $\alpha$  bond linking the hydroxyethylidene moiety to TPP has a much smaller influence on the EPR signals. The impression garnered from all of the data in Figure 1 is that none of the isotopic substitutions has a pronounced influence on the spectrum whereas all substitutions do have a modest influence on the spectrum. This circumstance is expected if there is extensive delocalization of the unpaired electron onto both the hydroxyethylidene and TPP moieties of the radical.



## EPR Spectral Simulations of the HE-TPP Radical

Experimental and simulated high-field EPR spectra of PFOR prepared with [3-<sup>2</sup>H<sub>3</sub>]pyruvate and unlabeled or [3-<sup>15</sup>N]TPP are shown in Figure 2. The EPR spectra are rhombic ( $g_x = 2.0079$ ,  $g_y = 2.0053$ ,  $g_z = 2.0021$ ). The anisotropy is expected to arise from significant spin density on S1 of the thiazolium ring (30). The  $g_z = 2.0021$  peak in the high-field EPR spectrum of the sample prepared with [3-<sup>15</sup>N]TPP is split into a doublet. This splitting results from an axially symmetric hyperfine interaction ( $|A_{\perp}| = 2\text{G}$ ,  $|A_{\parallel}| = 18\text{G}$ ) with the <sup>15</sup>N-nucleus ( $I = 1/2$ ). The corresponding triplet ( $I = 1$ ) <sup>14</sup>N-splitting in the high-field EPR spectrum of the sample prepared with unlabeled TPP ( $|A_{\perp}| = 1\text{G}$ ,  $|A_{\parallel}| = 13\text{G}$ ) is partially obscured due to the presence of a small amount of a contaminating free radical signal. The magnitude of the <sup>14</sup>N/<sup>15</sup>N-hyperfine splitting together with the axial symmetry indicates that there is significant  $\pi$ -spin density on N3 of the thiazolium ring.

In addition to the <sup>14</sup>N- or <sup>15</sup>N-hyperfine tensor, two isotropic hyperfine interactions ( $|A_{\text{iso}}| = 5\text{G}$ ,  $|A_{\text{iso}}| = 3\text{G}$ ) are required to account for all the peaks in the corresponding X-band EPR spectra of PFOR prepared with [3-<sup>2</sup>H<sub>3</sub>]pyruvate and unlabeled or [3-<sup>15</sup>N]TPP (Figure 3). These two doublet hyperfine interactions likely arise from one of the H-atoms from each of the two bridging methylene groups that link the pyrophosphate and amino-pyrimidine moieties to the thiazolium ring of TPP (5'-<sup>1</sup>H and 3'-<sup>1</sup>H, respectively). Isotropic <sup>1</sup>H-hyperfine splittings are a characteristic of  $\beta$ -proton hyperconjugation with an adjacent  $\pi$ -system (1). Such an interaction is expected if there is significant spin density at C5 and at N3 of the thiazolium ring. A significant amount of unpaired spin residing in the  $\pi$ -orbital at N3 is consistent with the axially symmetric <sup>14</sup>N/<sup>15</sup>N-hyperfine tensors.

The experimental and simulated X-band EPR spectra of PFOR incubated with unlabeled TPP and either unlabeled pyruvate or [3-<sup>13</sup>C]pyruvate are shown in Figure 4. To reproduce the features of the EPR spectrum obtained with unlabeled substrate and cofactor, two isotropic, doublet hyperfine splittings ( $|A_{\text{iso}}| = 10\text{G}$ ,  $|A_{\text{iso}}| = 5\text{G}$ ) were included. Since these splittings are not present in samples prepared with [3-<sup>2</sup>H<sub>3</sub>]pyruvate (Figure 3), these interactions arise from two of the three <sup>1</sup>H's of the C2 $\beta$ -methyl group of the hydroxyethylidene moiety.

Hyperconjugation follows a  $\cos^2\phi$  dependence, where  $\phi$  is the dihedral angle between the  $\beta$ -hydrogen and the normal to the thiazolium ring (1). The third <sup>1</sup>H-atom of the methyl group has an unfavorable dihedral angle for hyperconjugation. The <sup>1</sup>H-hyperfine interactions are similar in both number and magnitude to those obtained earlier from ENDOR spectroscopic measurements on PFOR from *M. thermoacetica* (2). These  $\beta$ -proton hyperfine interactions are most easily interpreted as arising from protons on a methyl group experiencing hindered rotation. The cryogenic temperature of the EPR measurement could, by itself, freeze rotation of the methyl group (31). The crystal structure of the *D. africanus* PFOR, however, shows that the methyl group of Thr 838 and one of the O-atoms of the tightly bound CO<sub>2</sub> molecule are within van der Waals contact of the C2 $\beta$ -methyl group of the substrate and could provide a barrier to free rotation (11).

Previous ENDOR results were interpreted in terms of two populations of radicals having different hyperfine couplings, but with both having rapid rotation of the methyl group at cryogenic temperatures (2). The alternative explanation to rapid rotation—namely that the two signals represented two <sup>1</sup>H-atoms having slightly different dihedral angles—was not considered. The ENDOR spectra were powder patterns having a slight anisotropy and powder patterns are not consistent with rapid methyl rotation. Rapid rotation was originally invoked to account for the fact that three <sup>1</sup>H-hyperfine couplings were not observed. However, as noted above, one of the <sup>1</sup>H-atoms of the methyl group must have an unfavorable dihedral angle if the other two are almost eclipsed with respect to the normal of the thiazolium ring. The weak hyperfine coupling of the third <sup>1</sup>H could easily escape detection by CW ENDOR. The latter explanation

also circumvents the problem of having to invoke an equilibrium between two forms of the radical having an equilibrium constant of unity.

The EPR spectrum obtained from samples prepared with [3- $^{13}\text{C}$ ]pyruvate contains additional splittings from hyperfine interactions with the  $^{13}\text{C}$ -nucleus ( $I = 1/2$ ). A relatively small isotropic hyperfine interaction ( $|A_{\text{iso}}| = 5\text{ G}$ ) was obtained from the simulations (Figure 4). Small isotropic  $^{13}\text{C}$ -hyperfine splittings are typical of  $\beta$ -carbons that experience spin polarization from a neighboring  $\pi$ -system (29). Thus, both the  $^1\text{H}$ - and  $^{13}\text{C}$ -hyperfine splittings from the C2 $\beta$ -methyl group of the hydroxyethylidene moiety are consistent with a radical structure in which there is significant  $\pi$ -spin density on the adjacent carbon atom (C2 $\alpha$ ).

To characterize further the HE-TPP radical structure, EPR spectra were acquired from samples prepared with [2- $^{13}\text{C}$ ]pyruvate or with [2- $^{13}\text{C}$ ]TPP (Figure 5). The  $^{13}\text{C}$ -hyperfine tensors obtained from simulations of these EPR spectra were both axially symmetric ( $|A_{\perp}| = 6\text{ G}$ ,  $|A_{\parallel}| = 18\text{ G}$  and  $|A_{\perp}| = 4\text{ G}$ ,  $|A_{\parallel}| = 9\text{ G}$  for  $^{13}\text{C}2\alpha$  and  $^{13}\text{C}2$  of the HE-TPP, respectively). The largest splitting comes from  $^{13}\text{C}2\alpha$  of the hydroxyethylidene moiety. The observation of substantial spin density at C2 $\alpha$  is compatible with the magnitudes of the  $^1\text{H}$ - and  $^{13}\text{C}$ -hyperfine splittings from the adjacent C2 $\beta$ -methyl group derived from the substrate. Although an earlier EPR study with [2- $^{13}\text{C}$ ]pyruvate in PFOR from *M. barkeri* (13) concluded that there was “negligible spin” at this position, this spectrum was not analyzed in detail. The spectrum from the *M. barkeri* PFOR sample prepared with [2- $^{13}\text{C}$ ]pyruvate in the earlier study (13) is virtually identical to that of *M. thermoaceticum* shown in Figure 1E. Both spectra exhibit inhomogeneous broadening from the unresolved  $^{13}\text{C}$ -hyperfine splitting. Extensive delocalization of spin onto the thiazolium moiety diminishes the magnitude of the  $^{13}\text{C}$ -hyperfine splitting from that expected for a central  $^{13}\text{C}$ -atom (1). An earlier electrochemical study of model thiazolium salts demonstrated formation of hydroxyethylidene radical cations that dimerized through C2 $\alpha$  (32). Thus, the electrochemical studies also support the notion of significant unpaired spin density at C2 $\alpha$ .

The  $g$ -values and hyperfine parameters obtained from the analysis of the CW EPR spectra of the HE-TPP radical are fully consistent with those expected for a  $\pi$ -radical in which spin is delocalized throughout the thiazolium ring and onto the substrate derived portion of the HE-TPP radical (33). The earlier observation of a weak, isotropic  $^{31}\text{P}$  hyperfine coupling (2) is also consistent with the extensive delocalization of spin. The  $^{31}\text{P}$ -nucleus is especially sensitive to small amounts of unpaired spin such that  $\sim 0.005\%$  unpaired spin<sup>2</sup> leaking into the  $2s$  orbital of phosphorus via spin polarization would account for the observed coupling (1).

Persistent cation radicals analogous to the HE-TPP radical have been generated via electrolysis of aldehyde derivatives of TPP analogs in acetonitrile (34). The isotropic  $g$ -values ( $g_{\text{iso}} = 2.0054$ ) and isotropic  $^{14}\text{N}$ -hyperfine splitting constants ( $a_{\text{N}} = 4.71\text{--}4.89\text{ G}$ ) reported for these model radicals in liquid solution are similar to the average  $g$ -value (2.0051) and isotropic  $^{14}\text{N}$ -splitting (5 G) obtained<sup>3</sup> from analysis of the spectra of the HE-TPP radical bound to PFOR. Similarities in these EPR parameters indicate that the enzyme does not appreciably distort the electronic structure of the HE-TPP radical from that of analogous species in liquid solution.

### Electronic Structure Calculations on Models of the HE-TPP Radical

To obtain further insight into the electronic structure of the HE-TPP radical, the EPR parameters obtained from the simulations were compared with those obtained from DFT

<sup>2</sup>The isotropic coupling calculated for an electron in a valence-shell  $s$  orbital on  $^{31}\text{P}$  is 10,178 MHz (1). The measured isotropic coupling (0.51 MHz) (2) thus corresponds to  $\sim 0.005\%$  of an unpaired spin in the  $2s$  orbital on phosphorus.

<sup>3</sup>The isotropic  $g$ -value and isotropic hyperfine splitting are given by 1/3 of the trace of the corresponding tensor.



calculations (Table 1-3) on various models of the HE-TPP radical structure (Scheme 1). As can be seen in Figure 6, the spin densities of the models that represent the postulated  $\sigma/n$ -type cation radicals (models 3/3' and 4/4') are actually more consistent with that of  $\pi$ -radicals. Models 3/3' are more accurately described as aza-allyl cation radicals. Addition of a proton to C2 of TPP effectively reduces delocalization of the unpaired electron onto the hydroxyethylidene portion of the HE-TPP radical, such that it cannot account for the  $^1\text{H}$ -hyperfine splittings that derive from the C2 $\beta$ -methyl group. Stretching the C2-C2 $\alpha$  bond to 1.95 Å (by freezing the heavy atoms of the radicals to the positions observed in the crystal structure), while increasing the spin density at C2 of TPP, actually decreases the spin density at C2 $\alpha$  and the  $^1\text{H}$ -hyperfine splittings remain far too small to be consistent with the values obtained from the experimental spectra. In addition, protonation at C2 increases the  $^1\text{H}$ -hyperfine splittings of the cofactor derived H-atoms, which would give rise to additional peaks not observed in the experimental EPR spectra. The calculated  $g_x$  and  $g_y$  values for model 3 are much smaller than those obtained from the spectra. Shifting the geometry of model 3 to that seen in the crystal structure (model 3') increases  $g_x$  and  $g_y$  to values closer to those obtained from the simulations, but simultaneously decreases  $g_z$  to too small a value. Conversely, model 4 has  $g_x$  and  $g_y$  values that are larger than seen in the D-band spectra, and shifting the geometry to that of model 4' has the effect of increasing  $g_x$  and  $g_y$  even further. Thus, it is clear that models 3/3' and 4/4' are not compatible with the EPR spectra of the radical intermediate in PFOR. Moreover, the electronic energies calculated for models in which the X-ray coordinates of heavy atoms were fixed (models 1' - 4') are  $\sim 100 \text{ kcal mol}^{-1}$  greater than those calculated for the corresponding geometry-optimized model (models 1 - 4).

It is also instructive to examine the RMSD<sup>4</sup> values between the geometry-optimized structures of the models and the heavy atom coordinates of the X-ray structure. The resulting superpositions are shown in Figure 7. The  $\pi$ -cation and neutral radicals (models 1 and 2) exhibit RMSD's of 0.4 Å whereas the  $\sigma/n$ -type cation radicals (models 3 and 4) exhibit RMSD's of 1.1 Å and 0.8 Å, respectively.

In contrast to the predictions of models 3/3' and 4/4', models 1 and 2 (which correspond to the protonated and unprotonated forms of the proposed HE-TPP  $\pi$ -radical, respectively) yield hyperfine parameters that more closely resemble those obtained from the analysis of the EPR spectra. However, model 1 overestimates the magnitude of the C2 $\beta$ - $^1\text{H}$ - and  $^{13}\text{C}2\alpha$ -hyperfine splittings. In contrast, model 2 leads to underestimates of these hyperfine splitting parameters. This situation suggests that the C2 $\alpha$  hydroxyl group of the HE-TPP radical is not fully protonated or deprotonated, but rather forms a hydrogen bond with a neighboring functional group. The most likely candidate to form a H-bond with the hydroxyl group is the exocyclic amino group from the pyrimidine moiety of the HE-TPP radical or the corresponding 1', 4'-imino tautomer (35,36). The presence of this intramolecular H-bond was revealed in the crystal structure, where the amino group was found to be 2.9 Å from the C2 $\alpha$  hydroxyl group of the HE-TPP radical (11). In addition to greatly elevating the electronic energies, restricting the heavy atoms of the radicals to the positions reported in the crystal structure (models 1' and 2') increases the magnitude of the  $^{13}\text{C}$ -hyperfine splitting derived from C2 of TPP such that these models cannot account for the more modest hyperfine splitting observed experimentally. In addition, the  $g_z$  values obtained from models 1' and 2' are much smaller than those obtained from the experimental spectra. Thus, the EPR properties of the radical intermediate of PFOR are fully compatible with an HE-TPP  $\pi$ -radical, whose geometry is consistent with a planar ground-state in which the unpaired electron is delocalized throughout the thiazolium ring and hydroxyethylidene moieties (models 1 and 2, Figure 6). The highly-delocalized  $\pi$ -radical electronic structure is also consistent with the known persistence of the radical even at room

<sup>4</sup>We are grateful to a reviewer for suggesting this comparison.

temperature (8). The  $^1\text{H}$ -hyperfine splittings of the C2 $\beta$ -methyl group and the  $^{13}\text{C}$ -hyperfine splittings of C2 and C2 $\alpha$  are part way between those predicted for the protonated (model 1) and unprotonated (model 2) structures of the HE-TPP radical which suggests that the hydroxyl group of the hydroxyethylidene moiety is H-bonded.

With regard to the possible mechanisms of the next steps in the PFOR reaction, the current study deems generation and fragmentation of a  $\sigma/\pi$ -type cation radical to an acetyl radical and subsequent radical recombination with a CoA thiol radical (11) unlikely, since the electronic structure of the HE-TPP radical is fully consistent with a  $\pi$ -radical. The electronic structures of the delocalized HE-TPP  $\pi$ -radicals (cation and neutral) render C2 $\alpha$  somewhat electropositive, perhaps promoting nucleophilic attack by the thiolate of CoA with consequent formation of a radical anion adduct (16). One-electron oxidation of such a radical anion would lead to formation of acetyl-CoA and release the second reducing equivalent into the electron transfer chain (16). An analogous scenario involving a radical anion intermediate has been suggested for the reaction of POX from *Lactobacillus plantarum* where  $\text{P}_i$  is the second substrate and acetyl-phosphate is the ultimate product (37). Equally plausible is CoA- ( $\text{P}_i$ -) gated oxidation of the HE-TPP radical, in which binding of a negatively charged thiolate (phosphate) in the active site could trigger the second electron transfer step in PFOR (POX) (16). Radical coupling involving a thiol radical (one electron oxidized) form of CoA might be possible in PFOR but such a scenario is not available for POX. Further experiments will be required to distinguish between these mechanisms for the subsequent steps in PFOR and other 2-keto acid oxidoreductases.

#### Acknowledgements

We thank Dr. Perry Frey for stimulating discussions and encouragement, and Dr. Russell Poyner for assistance with computing.

#### References

1. Wertz, JE.; Bolton, JR. Electron Spin Resonance. Chapman and Hall; New York: 1986.
2. Bouchev VF, Furdai CM, Menon S, Muthukumaran RB, Ragsdale SW, McCracken J. ENDOR Studies of Pyruvate:Ferredoxin Oxidoreductase Reaction Intermediates. J Am Chem Soc 1999;121:3724–3729.
3. Ragsdale SW. Pyruvate ferredoxin oxidoreductase and its radical intermediate. Chem Rev 2003;103:2333–2346. [PubMed: 12797832]
4. Chabriere E, Charon MH, Volbeda A, Pieulle L, Fontecilla-Camps JC. Crystal structures of the key anaerobic enzyme pyruvate:ferredoxin oxidoreductase, free and in complex with pyruvate. Nat Struct Biol 1999;6:182–190. [PubMed: 10048931]
5. Yakunin AF, Hallenbeck PC. Purification and characterization of pyruvate:ferredoxin oxidoreductase from the photosynthetic bacterium Rhodospirillum rubrum. Biochem Biophys Acta 1998;1409:39–49. [PubMed: 9804883]
6. Adams MW, Kletzin A. Oxidoreductase-type enzymes and redox proteins involved in fermentative metabolisms of hyperthermophilic Archaea. Adv Protein Chem 1996;48:101–180. [PubMed: 8791625]
7. Charon MH, Volbeda A, Chabriere E, Pieulle L, Fontecilla-Camps JC. Structure and electron transfer mechanisms of pyruvate:ferredoxin oxidoreductase. Curr Opin Struct Biol 1999;9:663–669. [PubMed: 10607667]
8. Cammack R, Kerscher L, Oesterheld D. A stable free radical intermediate in the reaction of 2-oxoacid:ferredoxin oxidoreductases of *Halobacterium halobium*. FEBS Lett 1980;118:271–273.
9. Cammack R, Patil DS, Fernandez VM. Electron-spin-resonance/electron-paramagnetic-resonance spectroscopy of iron-sulphur enzymes. Biochem Soc Trans 1985;13:572–578. [PubMed: 2993064]

10. Menon S, Ragsdale SW. Mechanism of the *Clostridium thermoaceticum* pyruvate:ferredoxin oxidoreductase: evidence for the common catalytic intermediacy of the hydroxyethylthiamine pyrophosphate radical. *Biochemistry* 1997;36:8484–8494. [PubMed: 9214293]
11. Chabriere E, Vernede X, Guigliarelli B, Charon MH, Hatchikian EC, Fontecilla-Camps JC. Crystal structure of the free radical intermediate of pyruvate:ferredoxin oxidoreductase. *Science* 2001;294:2559–2563. [PubMed: 11752578]
12. Kershner L, Oesterhelt D. Pyruvate:ferredoxin oxidoreductase-new findings on an ancient enzyme. *TIBS* 1982;7:371–374.
13. Bock AK, Schönheit P, Teixeira M. The iron-sulfur centers of the pyruvate:ferredoxin oxidoreductase from *Methanosarcina barkeri* (Fusaro). *FEBS Lett* 1997;414:209–212. [PubMed: 9315687]
14. Frey PA. 2-Acetylthiamin pyrophosphate: an enzyme-bound intermediate in thiamin pyrophosphate-dependent reactions. *Biofactors* 1989;2:1–9. [PubMed: 2679649]
15. Cavazza C, Contreras-Martel C, Pieulle L, Chabriere E, Hatchikian EC, Fontecilla-Camps JC. Flexibility of thiamine diphosphate revealed by kinetic crystallographic studies of the reaction of pyruvate-ferredoxin oxidoreductase with pyruvate. *Structure* 2006;14:217–224. [PubMed: 16472741]
16. Furdui C, Ragsdale SW. The roles of coenzyme A in the pyruvate:ferredoxin oxidoreductase reaction mechanism: rate enhancement of electron transfer from a radical intermediate to an iron-sulfur cluster. *Biochemistry* 2002;41:9921–9937. [PubMed: 12146957]
17. Frisch, MJ.; Trucks, GW.; Schlegel, HB.; Scuseria, GE.; Robb, MA.; Cheeseman, JR.; Zakrzewski, VG.; Montgomery, JJA.; Stratmann, RE.; Burant, JC.; Dapprich, S.; Millam, JM.; Daniels, AD.; Kudin, KN.; Strain, MC.; Farkas, O.; Tomasi, J.; Barone, V.; Cossi, M.; Cammi, R.; Mennucci, B.; Pomelli, C.; Adamo, C.; Clifford, S.; Ochterski, J.; Petersson, GA.; Ayala, PY.; Cui, Q.; Morokuma, K.; Malick, DK.; Rabuck, AD.; Raghavachari, K.; Foresman, JB.; Cioslowski, J.; Ortiz, JV.; Baboul, AG.; Stefanov, BB.; Liu, G.; Liashenko, A.; Piskorz, P.; Komaromi, I.; Gomperts, R.; Martin, RL.; Fox, DJ.; Keith, T.; Al-Laham, MA.; Peng, CY.; Nanayakkara, A.; Gonzalez, C.; Challacombe, M.; Gill, PMW.; Johnson, B.; Chen, W.; Wong, MW.; Andres, JL.; Head-Gordon, M.; Replogle, ES.; Pople, JA. Gaussian 98. A.9. Gaussian, Inc.; Pittsburgh, PA: 1998.
18. Neese, F. Max-Planck-Institut fuer Bioanorganische Chemie. Muelheim an der Ruhr; Germany: 2005.
19. Buchman ER. Crystalline vitamin B1 XIV sulfite cleavage 4 The thiazole half. *J Am Chem Soc* 1936;58:1803–1805.
20. Vernin, G. General synthetic methods for thiazole and thiazolium salts. In: Metzger, JV., editor. *Heterocyclic Compounds: Thiazole and Its Derivatives*. John Wiley & Sons; New York: 1979. p. 165-335.
21. Melnick JS, Sprinz KI, Reddick JJ, Kinsland C, Begley TP. An efficient enzymatic synthesis of thiamin pyrophosphate. *Bioorg & Med Chem Lett* 2003;13:4139–4141. [PubMed: 14592524]
22. Kauppinen JK, Moffatt DJ, Mantsch HH, Cameron DG. Fourier self-deconvolution: A method for resolving intrinsically overlapped bands. *Appl Spectrosc* 1981;35:271–276.
23. Latwesen DG, Poe M, Leigh JS, Reed GH. Electron paramagnetic resonance studies of a ras p21-Mn (II)GDP complex in solution. *Biochemistry* 1992;31:4946–4950. [PubMed: 1318075]
24. Burghaus O, Rohrer M, Plato M, Möbius K. A novel high-field/high-frequency EPR and ENDOR spectrometer operating at 3 mm wavelength. *Meas Sci Tech* 1992;3:765–774.
25. Bandarian V, Reed GH. Hydrazine cation radical in the active site of ethanolamine ammonia-lyase: Mechanism-based inactivation by hydroxyethylhydrazine. *Biochemistry* 1999;38:12394–12402. [PubMed: 10493807]
26. Goffe WL, Ferrier GD, Rogers J. Global optimization of statistical functions with simulated annealing. *J Econometrics* 1994;60:65–100.
27. Hermosilla L, Calle P, Garcia de la Vega JM, Sieiro C. Density functional theory predictions of isotropic hyperfine coupling constants. *J Phys Chem A* 2005;109:1114–1124. [PubMed: 16833420]
28. Hermosilla L, Calle P, Garcia de la Vega JM, Sieiro C. Theoretical isotropic hyperfine coupling constants of third-row nuclei (<sup>29</sup>Si, <sup>31</sup>P, and <sup>33</sup>S). *J Phys Chem A* 2005;109:7626–7635. [PubMed: 16834134]
29. Fischer, H. Structure of free radicals by ESR spectroscopy. In: Kochi, JK., editor. *Free Radicals*. Wiley; New York: 1973. p. 435-491.

30. Gordy, W. Theory and applications of electron spin resonance. Wiley-Interscience; New York: 1980.
31. Horsfield A, Morton JR, Whiffen DH. The electron spin resonance spectrum of  $\text{CH}_3\text{C}\cdot\text{HCOOH}$  at 77 K in L- $\alpha$ -alanine. *Molec Phys* 1961;4:425–431.
32. Barletta G, Chung AC, Rios CB, Jordan F, Schlegel JM. Electrochemical oxidation of enamines related to the key intermediate on thiamin diphosphate dependent enzymic pathways: evidence for one-electron oxidation via a thiazolium cation radical. *J Am Chem Soc* 1990;112:8144–8149.
33. Frey PA. Enzymology coenzymes and radicals. *Science* 2001;294:2489–2490. [PubMed: 11752561]
34. Nakanishi I, Itoh S, Suenobu T, Fukuzumi S. Electron transfer properties of active aldehydes derived from thiamin coenzyme analogues. *Chem Comm* 1997:1927–1928.
35. Jordon F. Interplay of organic and biological chemistry in understanding coenzyme mechanisms: example of thiamin diphosphate-dependent decarboxylation of 2-oxo acids. *FEBS Lett* 1999;457:298–301. [PubMed: 10471796]
36. Jordon F, Nemeria NS. Experimental observation of thiamin diphosphate-bound intermediates on enzymes and mechanistic information derived from these observations. *Bioorg Chem* 2005;33:190–215. [PubMed: 15888311]
37. Tittmann K, Wille G, Golbik R, Weidner A, Ghisla S, Hubner G. Radical phosphate transfer mechanism for the thiamin diphosphate- and FAD-dependent pyruvate oxidase from *Lactobacillus plantarum*. Kinetic coupling of intercofactor electron transfer with phosphate transfer to acetyl-thiamin diphosphate via a transient FAD semiquinone/hydroethyl-ThDP radical pair. *Biochemistry* 2005;44:13291–1303. [PubMed: 16201755]
38. Fluekiger, P., Luethi, H. P., Portmann, S., and Weber, J. (2002), Swiss National Supercomputing Centre, Manno, Switzerland.

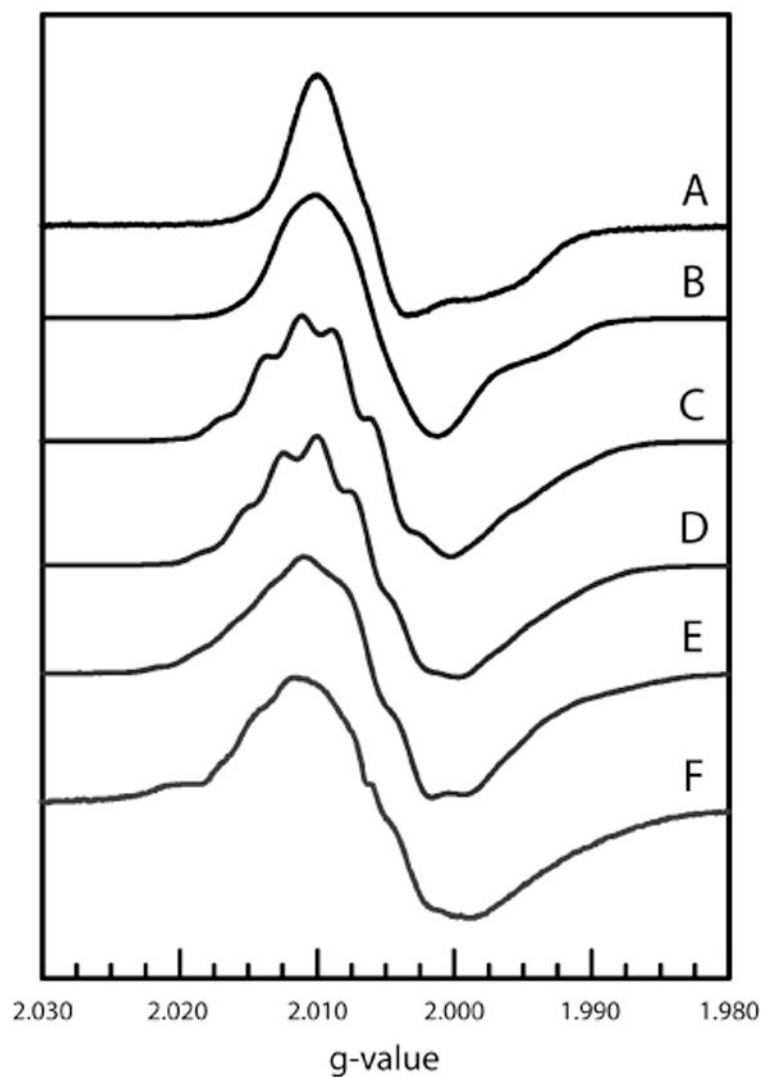


**Figure 1.**

Stack-plot of EPR spectra obtained from solutions of PFOR incubated with A)  $^{15}\text{N}_3$ -TPP and  $[3''\text{-}^2\text{H}_3]$ pyruvate, B) unlabeled TPP and  $[3''\text{-}^2\text{H}_3]$ pyruvate, C) unlabeled TPP and pyruvate, D) unlabeled TPP and  $[3\text{-}^{13}\text{C}]$ pyruvate, E) unlabeled TPP and  $[2\text{-}^{13}\text{C}]$ pyruvate, and F)  $^{13}\text{C}_2$ -TPP and unlabeled pyruvate. The experimental parameters were: temperature 80 K; receiver gain,  $5 \times 10^3$ ; modulation frequency, 100 kHz; modulation amplitude, 0.40 G; center field, 3400 G; sweep width, 100 G; microwave power, 0.4 mW; and number of scans, 32-64.



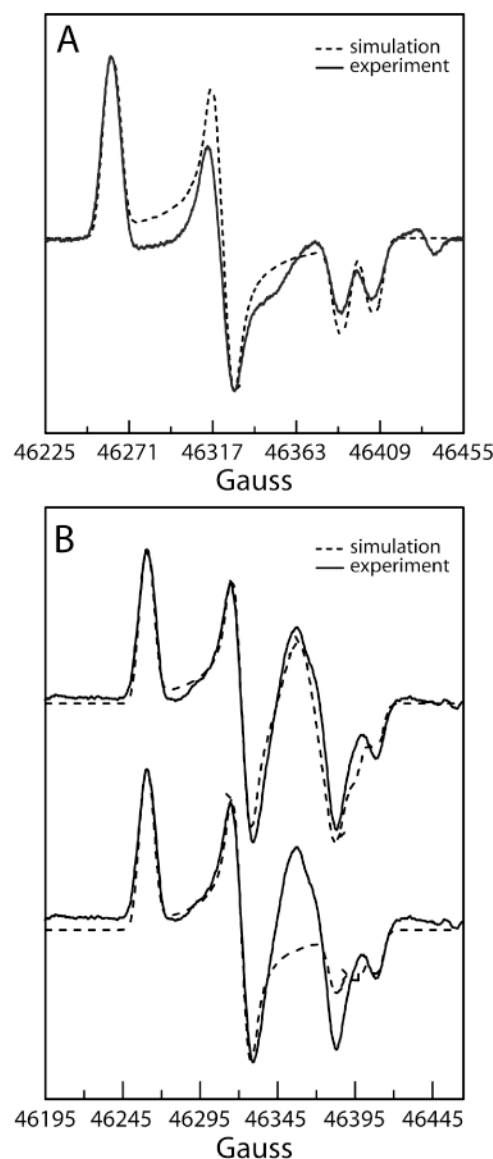


**Figure 2.**

Comparison of the experimental and simulated high-field EPR spectra of solutions of PFOR incubated with **A**)  $[3\text{-}^{15}\text{N}]\text{-TPP}$  and  $[3\text{-}^2\text{H}_3]\text{pyruvate}$  and **B**) unlabeled TPP and  $[3\text{-}^2\text{H}_3]\text{pyruvate}$ . Spectral simulations of **B**) were performed with and without inclusion of a contaminating free radical signal at a spin concentration of 15% that of the HE-TPP radical (upper and lower traces, respectively). The contaminant had a  $g$ -value of 2.0032 and a line width  $4\times$  greater than that of the HE-TPP radical. The experimental parameters for the D-band two-pulse echo-detected spectra were as follows: EPR frequency 129.9997 GHz; pulse widths, 50 ns; time between pulses, 120 ns; rep rate, 300 Hz; averages per data point, 300; temperature 50 K. The following parameters were used to simulate the spectra:  $g$ -tensor (2.0079; 2.0053; 2.0021); **A**)  $^{15}\text{N}$  hyperfine splitting tensor ( $|A_{\perp}| = 2\text{G}$ ,  $|A_{\parallel}| = 18\text{G}$ ); **B**)  $^{14}\text{N}$  hyperfine splitting tensor ( $|A_{\perp}| = 1\text{G}$ ,  $|A_{\parallel}| = 13\text{G}$ ). In **A**) and **B**),  $A_{\perp}$  was collinear with the  $g_{x,y}$  and  $A_{\parallel}$  was collinear with  $g_z$ . A line width of 3.5 G and Gaussian line shape were used.

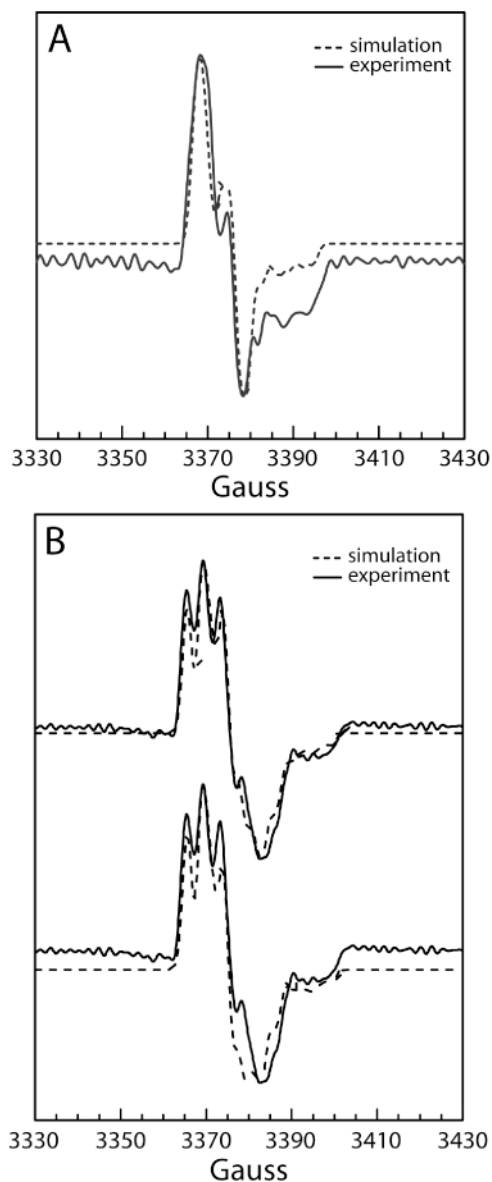


**Figure 3.**

Comparison of the experimental and simulated X-band EPR spectra of solutions of PFOR prepared with **A**)  $^{15}\text{N}_3\text{-TPP}$  and  $[3\text{-}^2\text{H}_3]\text{pyruvate}$  and **B**) unlabeled TPP and  $[3\text{-}^2\text{H}_3]\text{pyruvate}$ . Spectral simulations of **B**) were performed with and without inclusion of a contaminating free radical signal at a spin concentration of 15% that of the HE-TPP radical (upper and lower traces, respectively). The contaminant had a  $g$ -value of 2.0032 and a line width  $4\times$  greater than that of the HE-TPP radical. The resolution of the experimental EPR spectra in **A**) and **B**) was enhanced using cosine window functions with a line width of 3G and a truncation parameter of  $0.5\text{G}^{-1}$ . In addition to the  $g$  tensor and  $^{14,15}\text{N}$  hyperfine splitting tensors (see legend of Figure 2) two isotropic doublet splittings ( $|A_{\text{iso}}| = 5\text{G}$ ,  $|A_{\text{iso}}| = 3\text{G}$ ) were included. A linewidth of 1.3 G and Gaussian line shape were employed in the simulation.

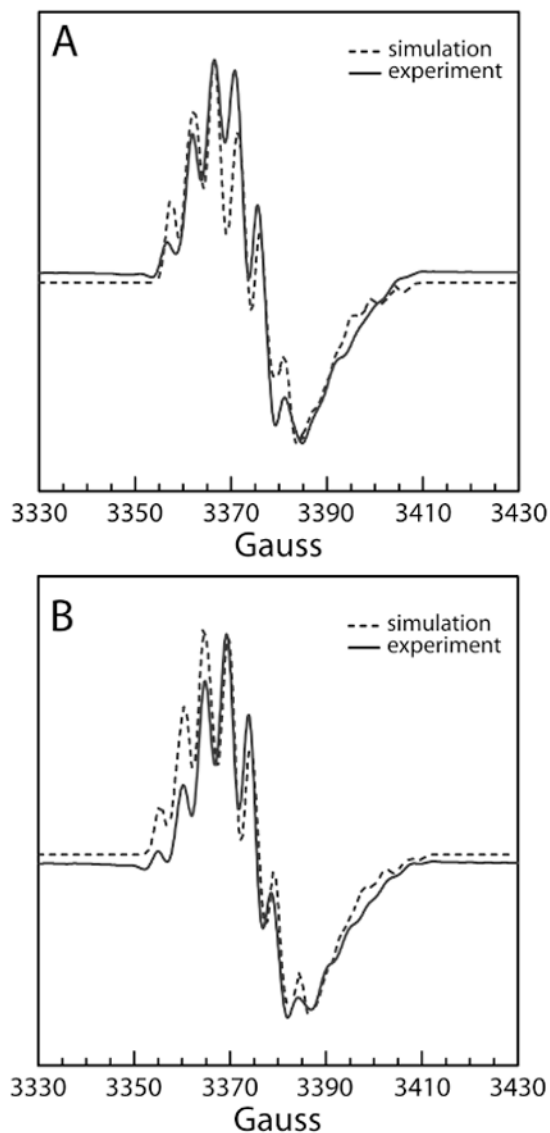


**Figure 4.**

Comparison of the experimental and simulated X-band EPR spectra of solutions of PFOR prepared with unlabeled TPP and **A**) unlabeled pyruvate and **B**) [ $3\text{-}^{13}\text{C}$ ]pyruvate. The resolution of the experimental EPR spectra in **A**) and **B**) was enhanced using cosine window functions with a line width of 2G and a truncation parameter of  $0.5\text{G}^{-1}$ . The simulations included the parameters listed in the legend of Figure 3. In **A**) and **B**), two isotropic, doublet hyperfine splittings ( $|A_{\text{iso}}| = 10\text{G}$ ,  $|A_{\text{iso}}| = 5\text{G}$ ) were included. In **B**) an isotropic doublet  $^{13}\text{C}$ -hyperfine splitting was included ( $|A_{\text{iso}}| = 5\text{G}$ ).

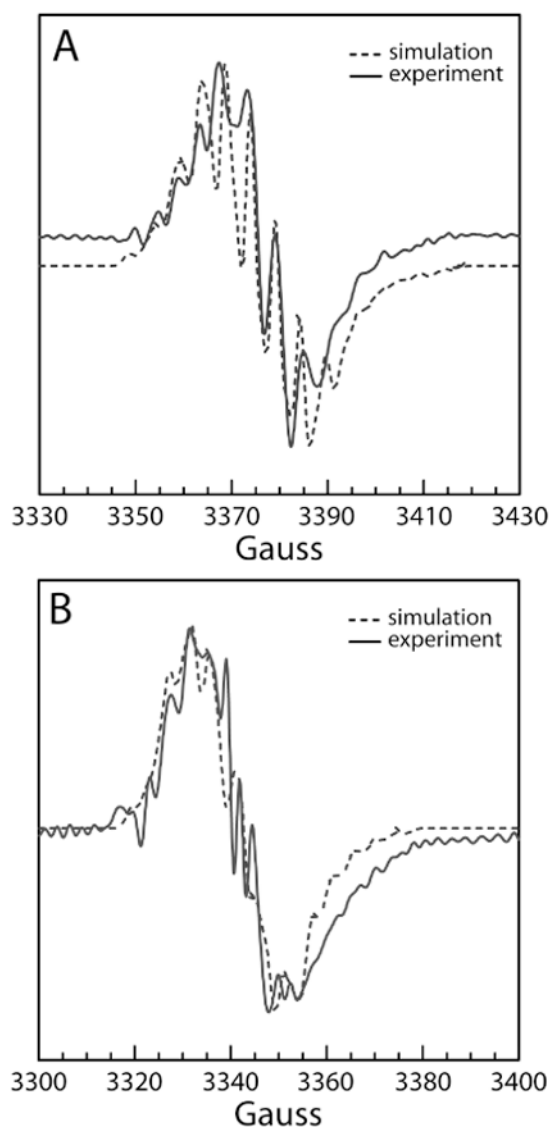


**Figure 5.**

Comparison of the experimental and simulated X-band EPR spectra of solutions of PFOR prepared with **A**) unlabeled TPP and [2-  $^{13}\text{C}$ ]pyruvate, and **B**)  $^{13}\text{C}_2$ -TPP and unlabeled pyruvate. The resolution of the experimental EPR spectra in **A**) and **B**) was enhanced using cosine window functions with a line width of 3G or 2G, respectively, and a truncation parameter of  $0.5\text{G}^{-1}$ . There is a small amount of contaminating signal evident in the EPR spectrum of **B**). However, attempts were not made to incorporate the contaminant into the simulations. The simulations included the parameters listed in the legend of Figure 3 and those in the legend of Figure 4A. In addition,  $^{13}\text{C}$  hyperfine splitting tensors: **A**) ( $|A_{\perp}| = 6\text{ G}$ ,  $|A_{\parallel}| = 18\text{ G}$ ) ; **B**) ( $|A_{\perp}| = 4\text{ G}$ ,  $|A_{\parallel}| = 9\text{ G}$ ) were included in the simulations.  $A_{\perp}$  is collinear with  $g_{xy}$  and  $A_{\parallel}$  is collinear with  $g_z$ .

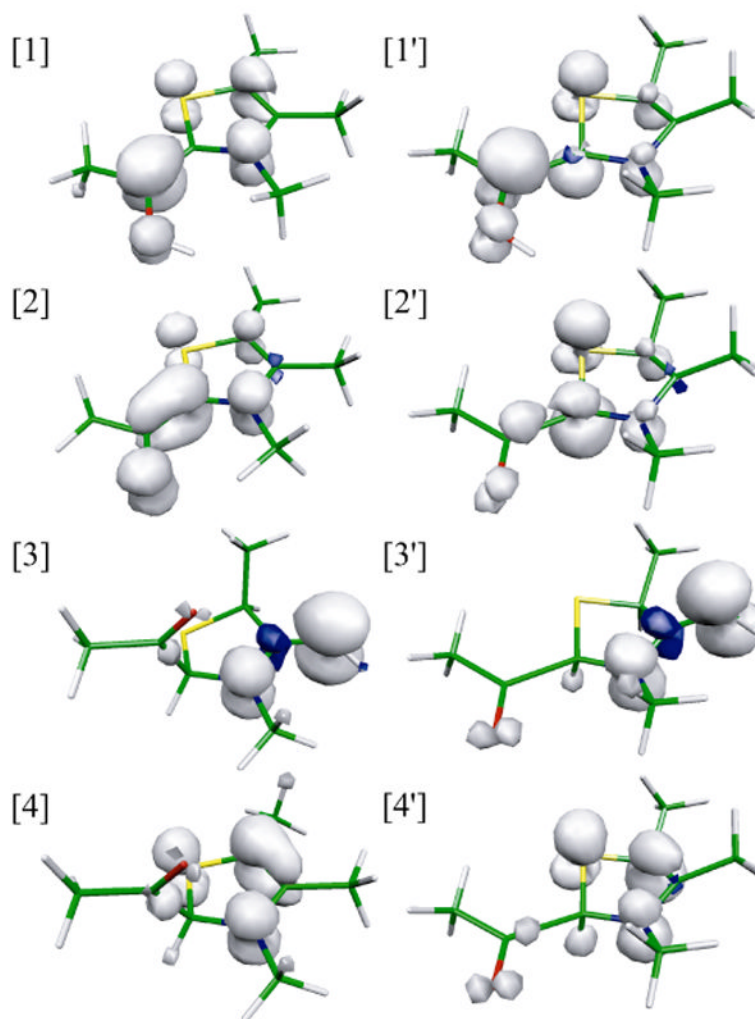


**Figure 6.**

Isosurface plots of the spin densities of different truncation models of the HE-TPP radical structure: [1] geometry-optimized protonated HE-TPP  $\pi$ -radical, [2] geometry-optimized unprotonated HE-TPP  $\pi$ -radical, [3] geometry-optimized HE-TPP  $\sigma/n$ -type cation radical, [4] geometry-optimized HE-TPP  $\sigma/n$ -type cation radical C5-C4' tautomer, [1'] protonated HE-TPP  $\pi$ -radical from X-ray coordinates (PDB code 1KEK), [2'] unprotonated HE-TPP  $\pi$ -radical from X-ray coordinates, [3'] HE-TPP  $\sigma/n$ -type cation radical from X-ray coordinates (11), [4'] HE-TPP  $\sigma/n$ -type cation radical C5-C4' tautomer from X-ray coordinates (15). Surface plots were generated with the program Molekel 4.3 (38) from the corresponding Gaussian log files using a cut-off of 0.005. Gray clouds represent positive spin density, and blue clouds represent negative spin density.



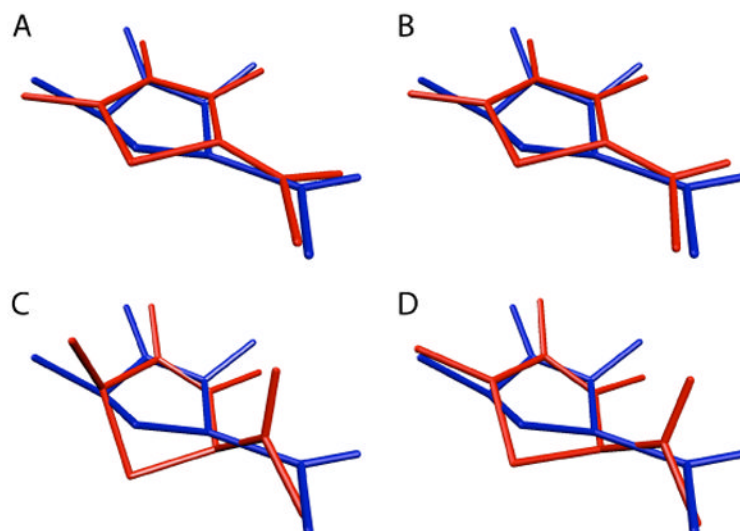
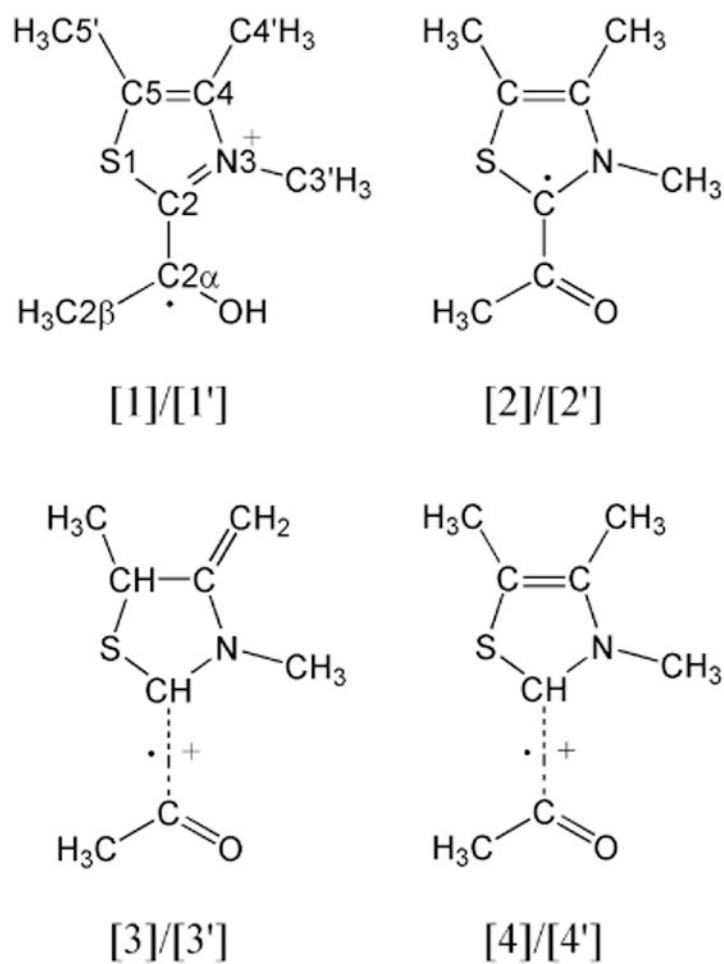


**Figure 7.**

Overlays of heavy atoms of geometry-optimized models of the HE-TPP radical (red) with X-ray coordinates (blue) from PDB accession code 1KEK (11): A) Protonated  $\pi$ -radical (model 1), RMSD 0.4 Å; B) Neutral  $\pi$ -radical (model 2), RMSD 0.4 Å; C)  $\sigma$ /n-type cation radical (model 3) (11), RMSD 1.1 Å; D) C5-C4' tautomer of  $\sigma$ /n-type cation radical (model 4) (15), RMSD 0.8 Å.



**Scheme 1.**  
Models used in electronic structure calculations.

Table 1

Comparison of experimental and calculated<sup>a</sup> hyperfine splitting tensors ( $|A_x|$ ,  $|A_y|$ ,  $|A_z|$  in Gauss) for the different models of the HETPP radical structure shown in Figure 6 of nuclei that were confirmed by isotopic substitution. Interactions that could be large enough to give rise to resolvable splittings are highlighted in bold.

Source	<sup>14</sup> N3	C2β- <sup>1</sup> H <sub>a</sub>	C2β- <sup>1</sup> H <sub>b</sub>	C2β- <sup>1</sup> H <sub>c</sub>	<sup>13</sup> C2β	<sup>13</sup> C2α	<sup>13</sup> C2
Experiment							
[1]	1,1,13	10,10,10	5,5,5	-	5,5,5	6,6,18	4,4,9
[2]	0,0,12	17,17,20	8,8,11	1,1,3	5,5,5	2,2,35	11,10,9
[3]	1,1,10	3,3,5	3,3,5	1,1,1	3,3,2	9,7,1	4,4,25
[4]	1,1,20	1,1,2	1,1,0	1,0,0	2,2,4	3,3,7	6,5,4
[1']	0,0,15	0,1,1	1,0,1	1,1,0	1,1,2	12,12,17	8,8,7
[2']	9,9,14	14,14,16	4,4,7	2,2,1	0,0,1	36,37,76	68,72,87
[3']	11,11,16	1,1,2	0,0,2	1,1,0	3,3,4	13,15,22	95,96,139
[4']	4,4,26	1,1,0	0,0,1	0,0,0	3,3,5	2,2,1	12,11,8
	8,8,19	0,1,2	1,1,0	1,1,0	4,5,7	3,3,7	13,12,10

<sup>a</sup> Calculations were performed with Gaussian 98.

Table 2

Comparison of the magnitude of experimental and calculated<sup>a</sup> <sup>1</sup>H-hyperfine parameters ( $|A_x|$ ,  $|A_y|$ ,  $|A_z|$  in Gauss) for the different models of the HETPP radical structure shown in Figure 6. Interactions that could be large enough to give rise to resolvable splittings are highlighted in bold.

Source	$b_{C3'-1H_a}$	$b_{C3'-1H_b}$	$b_{C5'-1H_a}$	$b_{C5'-1H_b}$	$C4'-1H_a$	$C4'-1H_b$	$C4'-1H_c$	$C2\beta-O-1H$	$C2-1H$	$C5-1H$
Experiment										
[1]	5,5,5	1,1,3	3,3,3	0,0,1	1,1,2	0,0,1	-	-	-	-
[2]	4,5,6	1,0,2	6,6,7	0,0,1	2,2,1	2,2,1	0,0,1	4,4,3	-	-
[3]	7,7,9	2,2,5	3,3,5	0,0,1	25,16,5	24,16,5	1,0,0	-	-	-
[4]	5,6,8	3,3,5	10,10,13	0,1,3	4,5,6	2,3,4	1,1,1	-	8,9,11	2,1,1
[1']	4,4,6	0,0,1	1,1,2	1,0,1	2,2,1	0,0,1	0,0,0	-	19,20,22	-
[2']	1,2,3	0,0,2	0,0,1	1,1,1	3,2,2	2,2,1	0,0,1	4,3,2	-	-
[3']	1,1,3	1,0,1	2,2,3	1,0,1	22,15,5	20,14,4	-	-	-	-
[4']	12,13,16	0,0,2	8,8,11	1,1,2	2,2,4	0,0,2	1,1,0	-	27,27,31	9,8,7
	8,9,11							-	43,43,46	-

<sup>a</sup>Calculations were performed with *Gaussian 98*.

<sup>b</sup>The C3' and C5' methylene groups (two <sup>1</sup>H's) of the HE-TPP radical are approximated by methyl groups (three <sup>1</sup>H's) in the truncation models. The largest <sup>1</sup>H-hyperfine splitting from these methyl groups was therefore omitted from the table for each of the models. This omission is consistent with the experimental EPR parameters and the binding mode of TPP observed in the crystal structure.

**Table 3**

Comparison of experimental and calculated<sup>a</sup>  $g$ -tensors for the Different models of the HETPP radical structure shown in Figure 6.

Source	$g_x$	$g_y$	$g_z$
Experiment	2.0079	2.0053	2.0021
[1]	2.0079	2.0060	2.0021
[2]	2.0094	2.0057	2.0020
[3]	2.0044	2.0034	2.0016
[4]	2.0094	2.0063	2.0019
[1']	2.0079	2.0043	1.9997
[2']	2.0082	2.0060	1.9985
[3']	2.0061	2.0044	2.0001
[4']	2.0110	2.0091	2.0022

<sup>a</sup> Calculations were performed with the program ORCA.